Electronic Supplementary Material (ESI) for Chemical Communications.

Electronic Supplementary Information

X-ray structural, functional and computational studies of the O_2-sensitive *E. coli* hydrogenase-1 C19G variant reveal an unusual [4Fe-4S] cluster.

A Volbeda, JM Mouesca, C Darnault, MM Roessler, A Parkin, FA Armstrong, JC Fontecilla-Camps

1. EPR characterization.

The C19G small subunit variant of *Escherichia coli* hydrogenase 1 (*Ec*Hyd1) was prepared, expressed, and purified as described before.[1,2,3] The solution redox titration of the *Ec*Hyd1 C19G variant and EPR measurements at both 15 and 80 K were carried out as described previously (**Fig. S1**).[2]

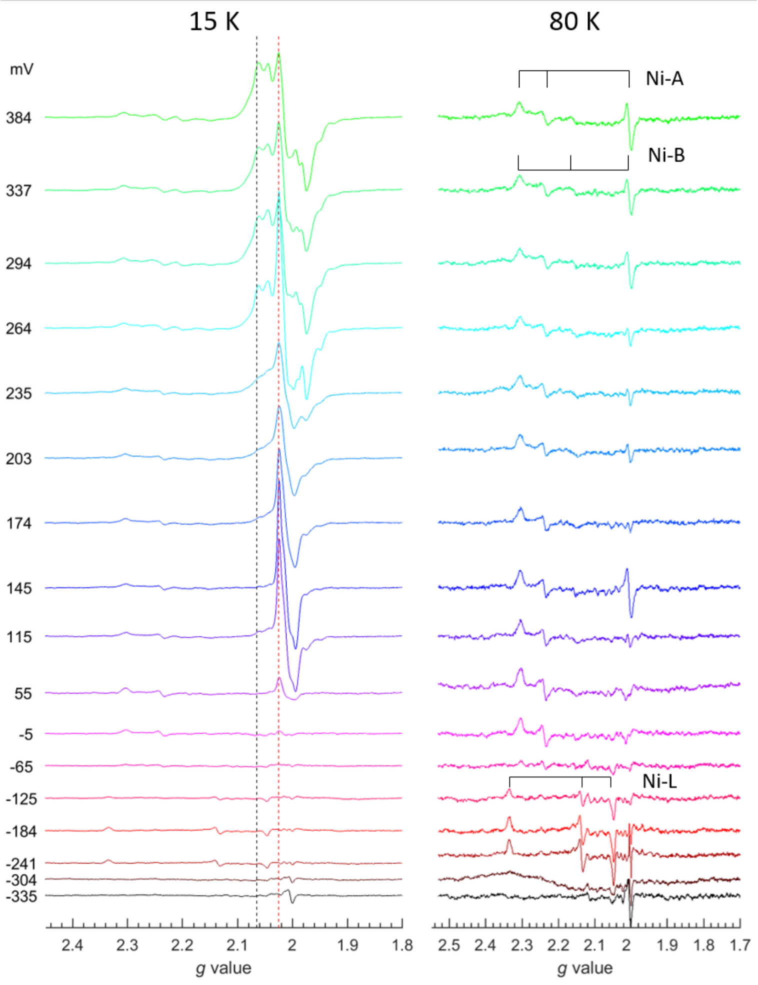

Figure S1. X-band CW EPR spectra of samples of *E. coli* Hyd-1 C19G at different potentials (more reducing, top to bottom) at 15 K (left) and at 80 K (right). Measurement conditions: microwave power 2 mW; modulation amplitude 1 mT; mw frequency 9.384-9.385 GHz; enzyme concentration: 16 µM. Annotations refer to the potential at which the sample was taken (in mV). The spin integration of the Fe-S cluster region was 2.1 ± 0.3 for the spectrum at +384 mV. Vertical lines at g = 2.025 and 2.065 indicate the peak heights monitored to extract mid-point potentials in a Nernst plot of the medial and proximal cluster (see **Fig. S2**). The sharp radical signal at $g \approx 2$ in some samples at 80 K results from redox mediators used in the titration.

---

[1] MJ Lukey *et al. J. Am. Chem. Soc.* **2011,** *133*, 16881.

[2] MM Roessler *et al. J. Am. Chem. Soc.* **2012,** *134*, 15581.

[3] RM Evans *et al. J. Am. Chem. Soc.* **2013,** *135*, 2694.

Similar to native Hyd-1, at the low temperature of 15 K the oxidized medial cluster is clearly visible at +145 mV. Upon increasing the potential, this simple Fe-S signal evolves into a more complex one that integrates to ~2 spins per molecule at maximal intensity. This complex signal is assigned to the magnetically coupled oxidized $[3Fe\text{-}4S]^+$ medial cluster and superoxidized (sox) $[4Fe\text{-}4S]^{-1}$ proximal cluster (PC_{sox}). The shape of the complex signal differs from that of native *Ec*Hyd1, but a correlated change in the behavior of the Ni signals (faster relaxation and splitting) and the $[3Fe\text{-}4S]^+$ signal indicates that the new paramagnetic species - that arises at high potential - is located between the medial cluster and the active site. We note that the formation of the coupled signal is not completely reversible in the C19G variant (for further details see the thesis "EPR investigations of Iron-Sulfur Cluster Relays in Enzymes" by MM Roessler, University of Oxford, 2011). No Fe-S cluster signals ($S = ½$) were observed at low potentials (**Fig. S1**).

At 80 K the Ni EPR signals of the C19G variant are observed uncoupled from the Fe-S relay, as is typical for a [NiFe]-hydrogenase. Such experiments show that the C19G variant gives rise to the same Ni EPR signals as the wild type (wt) enzyme, mostly corresponding to oxidized Ni-A, Ni-B and reduced Ni-L states (**Fig. S1**).

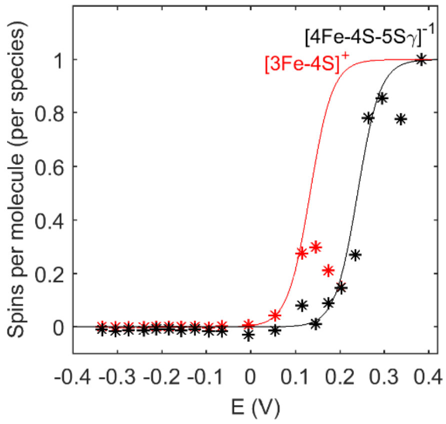

Figure S2. Peak intensities of the EPR active Fe-S species in the *Ec*Hyd1 C19G variant as a function of potential, fitted to the one-electron Nernst equation. Peak positions in the CW EPR spectra used to give the peak intensities are detailed in **Fig. S1** (left, dotted vertical lines). The maximum intensity of the medial cluster (at ~145 mV) was scaled on the basis of the sample at ~145 mV corresponding to 0.61 spin per molecule and the sample at +384 mV corresponding to 2.1 spins per molecule (see ref. 2). The assignment of the $[4Fe\text{-}4S\text{-}5S\gamma]^{-1}$ species ($S\gamma$ indicates a Cys thiolate ligand) is based on the crystal structure of the variant (see ESI section 2).

The peak intensities of the Fe-S cluster species observed in the EPR redox titration were used to generate the Nernst plot shown in **Fig. S2.** Data points were fitted to the one-electron Nernst equation and the redox potential of the medial cluster (solid red line in the figure) was determined on the basis of spin integration rather than from EPR signal intensities, as described previously.[2] Note that the intensity of the medial cluster EPR signal decreases as the coupled signal appears. The obtained midpoint potentials are +160±30 mV (compared to 190±30 mV in the wt)[2] and +240±15 mV (close to the superoxidation potential of 230±15 mV observed in the wt)[2] for the redox couples of the medial and proximal cluster, respectively.

2. Structure determination.

Crystals of the C19G small subunit variant (v) of *E. coli* hydrogenase 1 (*Ec*Hyd1) were anaerobically obtained as described before for the P242C variant.[4] A solution with a protein concentration of 5 mg mL^{-1} was prepared in 20 mM Tris/HCl pH 7.2, 150 mM NaCl, 1 mM dithiothreitol (DTT) and 0.02% n-dodecyl β-D-maltoside (DDM). Red-brown crystals (**Fig. S3A**) were obtained at room temperature by mixing 1 μL of this solution with 1 μL of a crystallization solution consisting of 12% PEG4000, 100

---

[4] A Volbeda *et al. Structure* **2013**, *21*, 184.

mM sodium acetate pH 5.7, 200 mM ammonium acetate, 1 mM DDT and 0.02% DDM and letting the resulting hanging drop equilibrate with the latter solution. Crystals were then transferred to a cryo-protectant solution of 35% PEG3350, 100 mM sodium acetate pH 5.7 and 200 mM ammonium acetate and then flash-cooled in liquid propane[5]. All these manipulations were carried out inside a glove box under a N_2 atmosphere. Next, the crystals were immediately stored in liquid nitrogen.

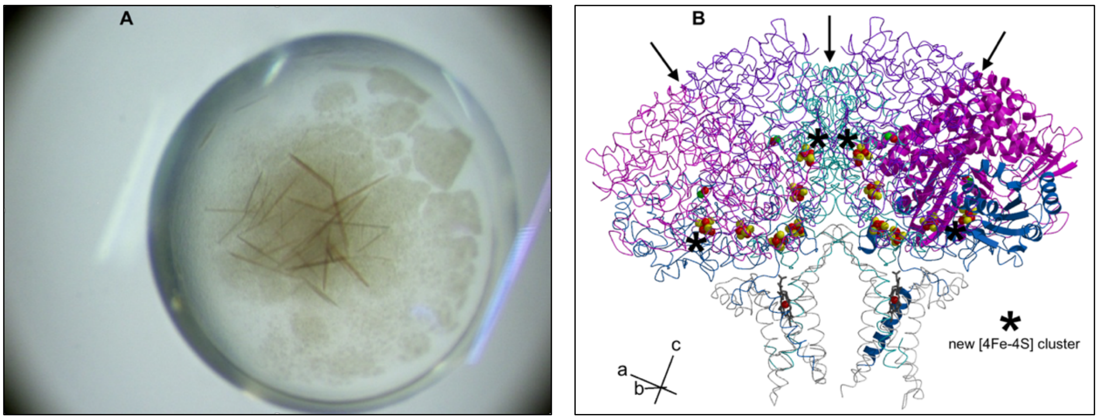

Figure S3. Crystals (**A**) and overall fold (**B**) of the C19G variant of *Ec*Hyd1. The asymmetric unit of the crystal contains four small (S), four large (L) and two intrinsic membrane cytochrome *b* subunits, which are shown in pink, blue and grey, respectively. One Hyd1 SL heterodimer is depicted with ribbons. Black arrows indicate three local twofold symmetry operations. For comparison, the directions of the **a**, **b** and **c** cell axes shown in the lower left corner. Black asterisks highlight proximal cluster (PC) positions.

Anisotropic X-ray diffraction data were collected with a Pilatus detector from a crystal kept under a cold (≈100 K) N_2 stream at beam line ID23-1 of the European Synchrotron Radiation Facility in Grenoble, France. The data were indexed and integrated with the XDS package[6] and further scaled with the program Aimless.[7] The structure was solved by molecular replacement with the program PHASER,[8] using the structure of the P242C variant[4] as a starting model. The asymmetric unit consists of 4 hydrogenase SL (S = small and L = large subunit) heterodimers packed against a dimer of cognate cytochrome *b* (B) subunits (**Fig. S3B**). Refinement of atomic positions and isotropic temperature factors was performed with Phenix,[9] followed by Refmac5,[10] including manual corrections with Coot.[11] In order to reduce the number of independently refined parameters and keep the different copies of the three types of subunits (S, L and B) nearly identical, torsion non-crystallographic symmetry (ncs) restraints were used during Phenix refinement. The latter were replaced by positional ncs restraints for the final cycles of refinement with Refmac5. In addition, TLS[9,10] bodies were defined for two domains of the S subunit (residues 3-172 and 173-266), the complete L subunit (2-582) and the B subunit (14-207) grouped together with its contacting trans-membrane helices from two different S subunits (267-299). Data collection and refinement statistics are summarized in **Table S1**.

Proximal cluster structural details were determined using four-fold averaged electron density maps, including averaged omit maps in which the inorganic cluster sulfide ions were not included in the model phases (**Fig. 1B** in main text). A four-fold averaged electron density omit map around the Ni-Fe site (**Fig. S4A**) indicates the presence of a putative water/hydroxide ligand, suggesting that the enzyme is in an oxidized state. A comparison of the obtained v-PC-X crystal structure (**Fig. S4B**) with the corresponding one in the O_2-sensitive [NiFe]-hydrogenase from *Desulfovibrio fructosovorans* and the previously characterized wt *Ec*Hyd1 PC-X crystal structures is shown in **Fig. S4C-F**.

---

[5] X Vernède & JC Fontecilla-Camps, *J. Appl. Cryst.* **1999**, *32*, 505.

[6] W Kabsch, *Acta Crystallogr. D Biol. Crystallogr.* **2010**, *67*, 235.

[7] PR Evans & GN Murshudov, *Acta Crystallogr. D Biol. Crystallogr.* **2013**, *69*, 1204.

[8] AJ McCoy *et al.*, *J. Appl. Cryst.* **2007**, *40*, 658.

[9] PV Afonine *et al.*, *Acta Crystallogr. D Biol. Crystallogr.* **2012**, *68*, 352.

[10] GN Murshudov *et al.*, *Acta Crystallogr. D Biol. Crystallogr.* **2011**, *67*, 355.

[11] P Emsley *et al.*, *Acta Crystallogr. D Biol. Crystallogr.* **2010**, *66*, 486.

Table S1. Crystallographic statistics for the *Ec*Hyd1 C19G variant.

X-ray diffraction data*		**Model refinement**	
Space group	$P2_12_12_1$	Resolution (Å)	25-2.5
Cell dimensions:		Work reflections	136263
a (Å)	124.4	R_{work} (%)	22.2
b (Å)	165.0	Test reflections	7064
c (Å)	206.2	R_{free} (%)	25.3
Subunits / asymmetric unit	$S_4L_4B_2$	Number of atoms	30463
Resolution (Å):	50-2.5 (2.56-2.5)	Fe	50
along a axis	3.7	Inorganic S	48
along b axis	2.5	Ni	4
along c axis	2.5	Mg	4
R_{merge}	0.259 (1.869)	Cl	4
$CC_{1/2}$	0.977 (0.279)	heme	2
<I>/<σ (I)>	6.5 (0.8)	water	702
Number of observations	656127 (64598)	σ_{bond} (Å)	0.010
Unique reflections	146009 (14192)	σ_{angle} (°)	1.20
Completeness (%)	99.4 (99.1)	average B (Å^2)	52.0
		<B_{PC}> (Å^2)$^\$$	44.8

* Numbers in parentheses refer to the highest resolution shell, $ average B factor of the new non-cubane proximal [4Fe-4S] cluster (using 32 atoms in 4 hydrogenase small subunits)

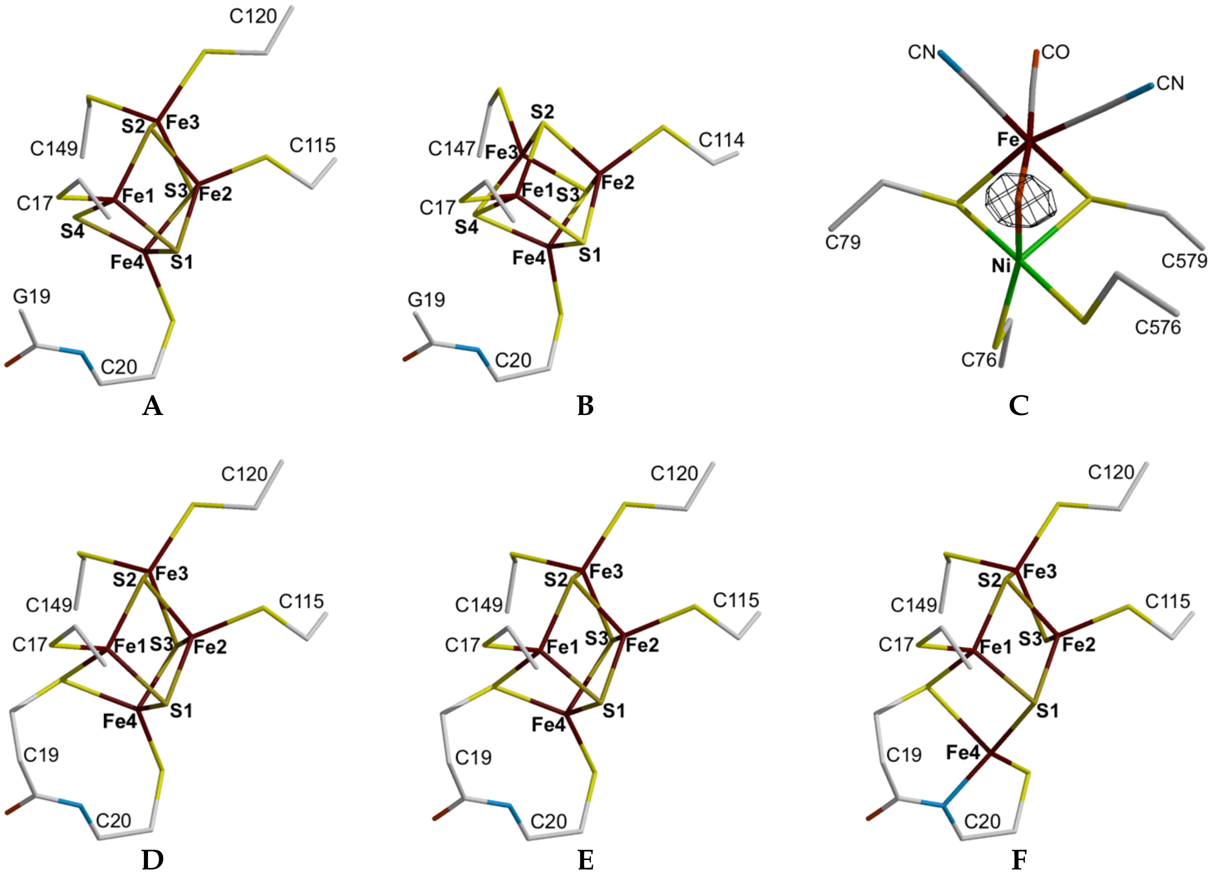

Figure S4. Selected metal sites in [NiFe]-hydrogenase crystal (-X) structures. (**A**) Proximal cluster (PC) of the *Ec*Hyd1 C19G variant (v), v-PC-X. Based on the used conditions this cluster can be in an oxidized state, a superoxidized state or a mixture of these two. (**B**) PC in the *Desulfovibrio fructosovorans* (*Df*) enzyme, *Df*-PC-X. (**C**) Active site of the *Ec*Hyd1 C19G variant (v) with four-fold averaged omit electron density map contoured at the 10 σ level suggesting the presence a Ni-Fe bridging hydroxide ligand**.** (**D**) Reduced (red) *Ec*Hyd1 PC in the wild type (wt), wt-PC_{red}-X state. (**E**) Oxidized (ox) wt-PC_{ox}-X. (**F**) Superoxidized (sox) wt-PC_{sox}-X.

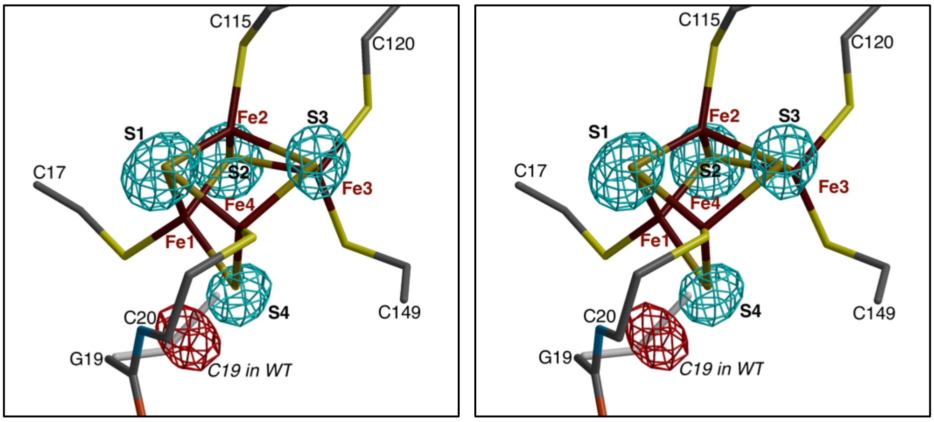

Figure S5. Stereo image of **Fig. 1B** of the main text. The red mesh indicates a negative peak, shown at the -8 σ level in a 4-fold density averaged F_{obs}-F_{calc} map calculated with phase information from a model including Cys19. The blue mesh, shown at the 20 σ level, corresponds to a 4-fold density averaged omit F_{obs}-F_{calc} map calculated with phase information from a C19G model excluding the inorganic S atoms.

3. DFT methodology.

All DFT calculations were performed with the ADF (Amsterdam Density Functional) code developed by E. J. Baerends and co-workers[12] using triple-zeta basis sets (no frozen core). Geometry optimizations were performed in water (ε=78) and then recalibrated to mimic protein environments (see **section 4.1**). This procedure has been applied to cubane-like [4Fe-4S-4Sγ] complexes (Sγ indicates here the thiolate ligand: SCH_2CH_3) of wt *Ec*Hyd1 and to C19G variant models, relying on the Generalized Gradient Approximation (GGA) VBP exchange-correlation (XC) potential (VWN + BP: Vosko, Wilk & Nusair[13] + corrective terms by Becke[14] for the exchange, and Perdew[15] for the correlation) with ADF grid precision 6 throughout.

$$\begin{tikzcd}
\mathbf{red(g)} \arrow[r, "\Delta G^\circ(\mathrm{red/ox})_{in}"] \arrow[d, "\Delta G^\circ(\mathrm{red})_{out}"'] & \mathbf{ox(g)} \arrow[d, "\Delta G^\circ(\mathrm{ox})_{out}"'] & + & \mathbf{e^-} \arrow[d, "\Delta G^\circ \equiv 0"] \\
\mathbf{red(w)} \arrow[r, "\Delta G^\circ(\mathrm{red/ox}) = -nF.E^\circ(\mathrm{red/ox})"'] & \mathbf{ox(w)} & + & \mathbf{e^-}
\end{tikzcd}$$

Scheme S1. Standard Born-Haber cycle for a redox reaction (cf. Eq. S1), with (g) and (w) corresponding to a gas phase and water environment, respectively.

To compute redox potentials E°_{DFT}(red/ox) relative to the Standard Hydrogen Electrode (SHE), we relied on the standard Born-Haber cycle **(Scheme S1)** for which the standard Gibbs free energy of a redox half reaction consists of the free energy change in the gas phase (ΔG_{in}) and the solvation free energies (ΔG_{out}) of the oxidized (ox) and reduced (red) species of a given redox couple[16,17]:

$$-nFE^\circ_{DFT}(\mathrm{red/ox})_{SHE} = \Delta G_{in} + \Delta G_{out} + \Delta G_{SHE} \qquad \text{(Eq. S1)}$$

More precisely, ΔG_{in} contains all contributions *intrinsic* to the cluster itself. These are:

---

[12] GT Velde & EJ Baerends, *J. Comput. Phys.* **1992**, *99*, 84.
[13] SH Vosko, L Wilk & M Nusair, *Canadian Journal of Physics*, **1980**, *58*, 1200.
[14] AD Becke, *Phys. Rev A*, **1988**, *38*, 3098.
[15] JP Perdew, *Phys. Rev. B*, **1986**, *33*, 8822.
[16] JM Mouesca *et al. J. Am. Chem. Soc*. **1994,** *116*, 11898.
[17] BS Perrin Jr & T Ichiye, *Proteins* **2010**, *78*, 2798.

i) the ionization energy of the reduced species, IE(red), which is computed as the enthalpic bonding energy (i.e. electronic internal energy) difference between the two redox partners, $\Delta E_B = E_B(ox)-E_B(red)$, with the VBP XC potential, following Noodleman *et al.*[18] and Batista *et al.*[19];
ii) the internal nuclear energy E_{int} which is the sum of the zero-point energy, 3 kT (i.e. (3/2) kT for translation and (3/2) kT for rotation, therefore (1/2) kT for each degree of freedom), and a small correction term due to the vibrational partition function;
iii) the entropic term $-T\Delta S$. This has been calculated for the cuboid [4Fe-4S-4Sγ] complexes as well as for the five wt and the five C19G models defined below, all for geometries optimized in water.

ΔG_{out} contains contributions from the interaction of the cluster with its polarizable environment. These contributions can be decomposed into (see Perrin & Ichiye[17]):
i) water (ε_w =78) solvation outside the protein;
ii) an average (ε_p =4) dielectric continuum for the protein environment;
iii) an explicit coulombic and backbone term (polarizable amide NH and carbonyl CO bonds);
iv) all remaining dipole contributions, including pH-dependent charges of protein residues.

All these terms will be discussed in the context of comparative calculations performed for [4Fe-4S-4Sγ] clusters. In Eq. S1, ΔG_{SHE} = -4.43 eV is defined at pH=0.[20] For higher pH values, ΔG_{SHE} increases by 0.059 eV per pH unit, so under standard physiological conditions at pH=7, ΔG_{SHE} shifts to -4.02 eV. We will show below how the calibration procedure we used to estimate redox potential values in proteins takes this shift (as well as the value assigned to ΔG_{SHE})[20] implicitly into account. Finally, F is the Faraday constant (here: 1 elementary electric charge) and n=1 for a one-electron reduction.
Solvation energies E_{env} have been computed with the COSMO (COnductor-like Screening MOdel)[21] ADF module, representing the solvent as a dielectric continuum. COSMO solvation energies behave according to a Born-like model, that is, they are proportional to Q^2 (the total cluster charge squared) multiplied by a factor of $(1-1/\varepsilon)$. We considered ε_w = 78 (ADF option: "solv name=water"), thus mimicking an average reaction field response of the environment (first step of the calibration procedure: see **section 4.1**). Solvation contributions to the final redox potentials are critical terms as their values depend drastically on the choice of ε. As we are interested in estimating the *relative* redox potential values of different Fe-S cluster variants within the same protein environment, we set up a strategy (section **4.1**) based on calculations for [4Fe-4S-4Sγ] clusters which, importantly, yields potentials close to experimental ones without having recourse to full QM/MM calculations.
The nomenclature used here for the different redox states and models is as follows. From an experimental point of view, we dispose of crystal structures for three functional redox states in the wt enzyme, called wt-PC_{red}-X, wt-PC_{ox}-X and wt-PC_{sox}-X (reduced, oxidized and superoxidized form, respectively). The main structural difference between wt-PC_{red}-X/wt-PC_{ox}-X and wt-PC_{sox}-X is the replacement of a Cys20N-H bond in the former by a deprotonated carboxamide N-Fe bond in the latter. For the C19G variant (v) we only have one crystal structure called v-PC-X. The presence of a peptide N-H or N-Fe bond is explicitly indicated in the names of the geometry-optimized models (**Scheme S2**):

---

[18] L Noodleman *et al.*, *J. Am. Chem. Soc.* **2003**, *125*, 1923.
[19] LE Roy, ER Batista & PJ Hay, *Inorg. Chem.* **2008**, *47*, 9228. See also LE Roy, E Jakubikova & ER Batista: www.researchgate.net/file.PostFileLoader.html?id=56673ec760614bd8848b4568&assetKey=AS%3A304487376326658%401449606855955
[20] Following ref. 18 and H Reiss & A Heller, *J. Phys. Chem.* **1985**, *89*, 4207. Other authors recommend a value of -4.28 eV for theoretical DFT calculations. See discussion in CP Kelly *et al.*, *J. Phys. Chem. B* **2006,** *110,* 16066; CP Kelly *et al., J. Phys. Chem. B* **2007,** *111,* 408; AA Isse & A Gennaro, *J. Phys. Chem. B* **2010**, *114,* 7894.
[21] (a) A Klamt & G Schürmann, *J. Chem. Soc. Perkin Trans. 2*, **1993**, 799. (b) A Klamt, *J. Phys. Chem.* **1995**, *99*, 2224. (c) A Klamt & V Jona, *J. Chem. Phys.* **1996**, *105,* 9972.

$$\begin{tikzcd}
\text{wt-pc}_{\text{red}}\text{-NH}^{-3} \arrow[d, "\text{ox } (-\,e^-)"] & \\
\text{wt-pc}_{\text{ox}}\text{-NH}^{-2} \arrow[r, "-H^+"] \arrow[d, "\text{ox } (-\,e^-)"] & \text{wt-pc}_{\text{ox}}\text{-NFe}^{-3} \arrow[d, "\text{ox } (-\,e^-)"] \\
\text{wt-pc}_{\text{sox}}\text{-NH}^{-1} \arrow[r, "-H^+"] & \text{wt-pc}_{\text{sox}}\text{-NFe}^{-2}
\end{tikzcd}$$

Scheme S2. Chemical relationships between geometry-optimized models of wt *Ec*Hyd1, including their total charges as exponents. In red: structures derived from crystallography. For the variant (with different total charges, see section 4.4) "wt" is replaces by "v".

In order to compare computed redox potential values at the same DFT methodology level, we considered five geometry-optimized models for wt: protonated wt-pc$_{red}$-NH, wt-pc$_{ox}$-NH, wt-pc$_{sox}$-NH and deprotonated wt-pc$_{ox}$-NFe and wt-pc$_{sox}$-NFe. **Scheme S2** summarizes the five geometry-optimized structures for wt as well as their relationships.

CAVEAT: In principle for both wt and C19G we need two diamagnetic broken-symmetry (BS) Ms=0 states, i. e., the pc$_{ox}$-NH and pc$_{ox}$-NFe redox states (see labels above) and three paramagnetic BS Ms=1/2 states, i. e., pc$_{red}$-NH, pc$_{sox}$-NH and pc$_{sox}$-NFe, which gives a total of 10 BS states combining wt and C19G data. There are three possible spin arrangements for each Ms=0 BS state corresponding to three possible locations of a mixed-valence pair among the four iron atoms (see **Fig. 2** in main text): 1-2/3-4, 1-3/2-4 and 1-4/2-3, and for each Ms=1/2 BS state there are six possible locations of a ferrous or ferric pair among four iron atoms: 1-2, 1-3, 1-4, 2-3, 2-4 and 3-4. This would amount to $2 \times 3 + 3 \times 6 = 24$ geometry-optimization per system (wt & C19G), and therefore a total of 48 calculations.

Based on previous investigations, we chose to perform all DFT calculations for only two BS states. The first one is BS13, obtained by flipping the local spin of irons 1 & 3. This BS13 state has been shown[22] to best describe the ground state of the wt-PC$_{sox}$ proximal cluster. The BS13 state was also previously chosen to describe the diamagnetic wt-PC$_{ox}$ redox state because in the absence of additional experimental data there were not enough structural differences to discriminate between the three possible BS states. We then computed BS13 states for the wt-pc$_{red}$ models. The second BS state is BS12, as Pelmenschikov & Kaupp[23] found by QM/MM calculations for their various pc$_{red}$ and pc$_{sox}$ models that this state was the lowest (or almost the lowest) in energy among the six available BS alternatives (Table S5 in their SI; with same iron atom labels as ours). These authors also computed minima and transition states for BS13 and found that it provides an almost identical energy profile to that computed for BS12 (Fig. S4 in their SI).

We have therefore duplicated our calculations for BS12 and BS13 states, resulting in 20 geometry-optimizations, i.e. 2×5 for the wt (see also **Scheme S2**) and 2 x 5 for the variant. However, in order to shorten and simplify the description of our results and their discussion we only report the calculated "vertical" redox potentials pertaining to the lowest BS states for each system (wt & C19G) and corresponding state.

4. Vertical redox potential calculations.

4.1. Calibration procedure based on [4Fe-4S] ferredoxins versus [4Fe-4S-4Sγ] models.

1) In O$_2$-tolerant wt *Ec*Hyd1 the proximal cluster yields two electrons at relatively high but close potentials: **+0.03 V** (**PC**$_{red}$/PC$_{ox}$) and **+0.23 V** (PC$_{ox}$/PC$_{sox}$) measured at pH=6 (ref.2). Its protein environment is very close to that of O$_2$-sensitive hydrogenases, for which the proximal cluster yields only one electron at a typically more negative (**PC**$_{red}$/PC$_{ox}$) redox potential ($E°$) of -0.29 or -0.34 V for

---

[22] A Volbeda *et al.*, *Proc. Natl. Acad. Sci. USA* **2012**, *109*, 5305.

[23] V Pelmenschikov & M Kaupp, *J. Am. Chem. Soc.* **2013**, *135*, 11809.

Desulfovibrio gigas[24] and -0.34 V for *D. fructosovorans*.[25] These [4Fe-4S] redox potentials are similar to the -3/-2 redox couple of standard ferredoxins (Fds), whereas the ones for O_2-tolerant hydrogenases are closer to the -2/-1 redox couple of high potential iron-sulfur protein (HiPIP) [4Fe-4S] clusters (**Table S2**). Recently, Perrin and Ichiye (2010)[17] compared experimental and DFT results for the two redox potentials of standard [4Fe-4S] clusters in proteins from several organisms. In the case of the Fd center from *Clostridium pasteurianum* the measured *E*°'s are **-0.41 V** in reduction (-3/-2)[26] and **+0.73 V** in oxidation (-2/-1 apparent value); it should be noted that the -1 state is unstable and that the real superoxidation potential is estimated to be at least 0.86 V.[27] For the HiPIP center from *Rhodopila globiformis* the measured *E*°'s are **-0.91 V** in reduction and **+0.43 V** in oxidation (**Table S2**).[28]

2) For the sake of comparison and calibration, we computed the (-3/-2) and (-2/-1) redox potentials of [4Fe-4S-4Sγ] models[29] [Sγ from SCH_2CH_3 ligand] corresponding to PC_{red}/PC_{ox} and PC_{ox}/PC_{sox} couples. We first geometry-optimized these models within the water dielectric continuum. We subsequently computed gas-phase energies for these optimized geometries, as well as internal energies and entropic terms (i.e. –TS at T=298.15 K) for the three redox states. The resulting redox potential values for these [4Fe-4S-4Sγ] complexes in water are shown in **Table S3**.

Table S2. Comparison between environment (i.e. solvation) contributions and redox potentials for: i) Fds and HiPIPs data taken from Perrin & Ichiye[17] (their Table 1) and ii) redox potential values for O_2-sensitive and O_2-tolerant hydrogenases. Note that we ranged both oxidation potentials of the O_2-tolerant proximal system within the (-3/-2) class, as it will be shown below that they both correspond to a (-3/-2) redox couple.

Redox couples	**HiPIPs**			**Fds**			**O_2-sensitive hydrogenases**	**O_2-tolerant hydrogenases**
	ΔE_{in} (eV)	**ΔE_{out} (eV)**	***E*°$_{exp}$ (V)**	**ΔE_{in} (eV)**	**ΔE_{out} (eV)**	***E*°$_{exp}$ (V)**	***E*°$_{exp}$ (V)**	***E*°$_{exp}$ (V)**
(-3/-2)	-3.48	+7.13	**-0.91**	-3.48	+7.32	**-0.41**	-0.29/-0.34	+0.03 & +0.23
(-2/-1)	+0.26	+4.43	**+0.43**	+0.26	+4.62	**+0.73**	n.d.	n.d.

Table S3. Total charge Q, bonding energies E_B, internal energies E_{int}, entropic terms -TS (at 298 K), solvation energies $E_{env}(w)$ (w indicating a water environment), free energies G (= E_B +E_{int} –TS +$E_{env}(w)$), ΔE_{in} (= ΔE_B + ΔE_{int} -TΔS, to be compared with Perrin & Ichiye's data; cf. Table S2) and calculated *E*°$_{DFT}$ redox potentials for geometry-optimized [4Fe-4S-4Sγ] models in a dielectric water continuum (ε_w=78). Using ε=80, Noodleman *et al.*[18] computed -0.89 V and -0.11 V for the (-3/-2) and (-2/-1) redox couples (electronic states of lowest energies).

[4Fe-4S] $(SCH_2CH_3)_4$	**Q**	**E_B (eV)**	**E_{int} (eV)**	**-TS (eV)**	**$E_{env}(w)$ (eV)**	**G (eV)**	**ΔE_{in} (eV)**	**$\Delta E_{env}(w)$ (eV)**	***E*°$_{DFT}$ (V)**	***E*°(ref.18) (V)**
"PC_{red}"	-3	-213.59	+8.09	-2.61	-14.31	-222.42	-4.00	+7.72	-0.71	-0.89
"PC_{ox}"	-2	-217.62	+8.19	-2.68	-6.59	-218.70	-0.20	+4.72	+0.09	-0.11
"PC_{sox}"	-1	-217.82	+8.28	-2.77	-1.87	-214.18				

---

[24] M Teixeira *et al., J. Biol. Chem.* **1989**, *264*, 16435

[25] M Rousset *et al., Proc. Natl. Acad. Sci. USA* **1998**, *95*, 11625.

[26] G Battistuzzi *et al., J. Biol. Inorg. Chem.* **2000**, *5*, 748.

[27] FA Armstrong, HAO Hill & NJ Walton, *FEBS Lett.* **1982**, *150*, 214.

[28] HA Heering, YBM Bulsink, WR Hagen & TE Meyer, *Eur. J. Biochem.* **1995**, *232*, 811.

[29] See also calculations by Mouesca *et al.* (ref. 16) for ε= 80; Noodleman *et al.* (ref. 18) for ε=80.

From the data in **Tables S2** and **S3** it can be noticed that experimental values and trends are reasonably well reproduced by calculations. Our values are shifted by -0.19 V compared to Noodleman's values (ref.18), but this has no consequence (see below). More importantly, $\Delta E_{env}(w)$ terms computed for a $\varepsilon_w = 78$ water dielectric continuum surrounding the cluster are *quantitatively* close to the ΔE_{out} terms computed by Perrin & Ichiye[17] for Fds and HiPIPs, although these include four types of contribution (see **DFT Methodology** section above). As discussed by these authors[17] (see their Figures 3-4), solvation terms coming from water modelled as a dielectric continuum *outside* the protein and dielectric continuum $\varepsilon_p = 4$ *inside* the protein account *each* for ~40-45 % of their ΔE_{out}. In other words, the dominant dielectric continuum terms accounting for 80-90% of the environment terms are scalable by factors of the form $(1\text{-}1/\varepsilon)$. The minor contributions coming from all explicit polarizable bonds (including those in charged amino acid residues) account for the comparatively minor but determining differences between Fds and HiPIPs.

The semi-quantitative agreement between Perrin & Ichiye's ΔE_{out} values (**Table S2**) and our $\Delta E_{env}(w)$ values (**Table S3**) suggests that the computation of $\Delta E_{env}(w)$ terms might be a good starting point for the computation of redox potentials for the wild-type and C19G mutant proximal clusters. Similarly, MHM Olsson, JH Jensen *et al.*[30] started their empirical computation of pKa values (for $AH \rightarrow A^- + H^+$) in proteins from pKa's computed in water, further correcting them when moving the AH/A^- residues from water to protein environments (PROPKA3 model). In our case, this strategy translates into:

$$\Delta E_{env}(\text{protein}) = \Delta E_{env}(w) + \delta E_{env}(w \rightarrow \text{protein}) \equiv (1+x)\Delta E_{env}(w) \qquad \text{(Eq. S2)}$$

In Eq. S2, $\Delta E_{env}(w)$ will be computed by DFT via the COSMO module and the corrective term δE_{env} expressed as $x \cdot \Delta E_{env}(w)$ will correct for the environment change from water to protein. Using the Born model we define the quantity $\Delta E_{env}(\infty) = \Delta E_{env}(w)/(1\text{-}1/\varepsilon_w) = (Q_{red}^2\text{-}Q_{ox}^2)/(2R_c)$ where R_c is the radius of the redox site, here for the red/ox couple. Similarly, for the protein we define:

$$\Delta E_{env}(\text{protein}) = (Q_{red}^2\text{-}Q_{ox}^2)/(2R_c) \times (1\text{-}1/\varepsilon_{av}) \qquad \text{(Eq. S3)}$$

In Eq. S3, ε_{av} stands for an adjustable dielectric constant (see below) that accounts for the *average* reaction field created by the whole dielectric environment. The value of ε_{av} is therefore expected to be comprised between $\varepsilon_p = 4$ (protein interior) and $\varepsilon_w = 78$ (water). It can be easily shown from Eq. S2 and S3 that $x = (\varepsilon_{av} - 78)/(77.\varepsilon_{av}) \Leftrightarrow \varepsilon_{av} = 78/(1 - 77 \cdot x)$, hence $-0.24 \leq x \leq 0$ for $4 \leq \varepsilon_{av} \leq 78$. The reason behind introducing the corrective term via x will become clear below. In the meantime, we should keep in mind that $x(\varepsilon_{av})$ reflects directly the cluster's average dielectric environment via ε_{av}. We can further link our approach with that of Perrin and Ichiye[31] by comparing our Eq. S3 with their eq. 3 (ref.31):

$$\Delta E_{env}(\text{protein}) = (Q_{red}^2\text{-}Q_{ox}^2) \times [(1\text{-}1/\varepsilon_p)/(2R_c) + (1/\varepsilon_p \text{-}1/\varepsilon_w)/(2R_p)] \qquad \text{(Eq. S4)}$$

In Eq. S4, R_p is the dielectric radius of the protein around the cluster. By equating Eqs. S3 and S4, it can then be shown that: $(R_p/R_c) = (\varepsilon/\varepsilon_w) \times (\varepsilon_w\text{-}\varepsilon_p)/(\varepsilon_{av}\text{-}\varepsilon_p)$. From our DFT-derived value $R_c = 4.57$ Å obtained from plotting $E_{env}/(1\text{-}1/78)$ (Table S3) as a function of Q^2 for [4Fe-4S-4Sγ] models and, for Fds, $R_p = 8.9$ Å (ref.31), one would deduce $\varepsilon_{av} = 7.8$ (which is indeed comprised between 4 and 78).

3) The difference between (-3/-2) redox potentials computed for [4Fe-4S-4Sγ] complexes in water and experimental values for Fds or oxygen-sensitive hydrogenases is about **0.5 V**. However, one cannot use the same constant corrective shift for redox potentials corresponding to different cluster total charges because $E_{env}(w)$ is proportional to Q^2 (Born model). Instead, one can rely on a calibrated correction for both redox couples by adjusting the environmental continuum dielectric term (via

---

[30] M. H. M. Olsson, C. R. Sondergaard, M. Rostkowski and J. H. Jensen, *J. Chem. Theory Comput.* **2011**, *7*, 525-537.

[31] BS Perrin and T Ichiye, *J. Biol. Inorg. Chem.* **2013**, *18*, 103-110.

$x(\varepsilon_{av})$: cf. Eq. S2) and by adding a shift (y) resulting from an environment term varying linearly with the cluster charge Q (i.e. the $Q\Phi_p$ term in eq. 3 of ref.31):

$$E°_{exp} = E°_{DFT} + [x\cdot\Delta E_{env}(w) + y]/F \qquad \text{(Eq. S5)}$$

The y term in Eq. S5 contains (but is not identical to) Perrin & Ichiye's Φ_p, the so-called protein electret potential defined as the average electrostatic potential at the redox site. For Fds, Perrin & Ichiye compute Φ_p = 0.59 eV (Table 1 in ref.31). In our case, the value of y will be obtained by solving a set of two linear equations. As a result, it also contains corrective terms due to uncertainties in the computed contributions to $E°_{DFT}$. For example, Perrin & Ichiye's ΔG_{in} terms of -3.48 eV and +0.26 eV for Fd(-3/-2) and Fd(-2/-1) redox couples (Table S2), respectively, are ≈0.5 eV higher than our ΔG_{in} terms of -4.00 eV and -0.20 eV (Table S3). It also contains a correction for Φ_p, as well as any additional electrostatic term not taken into account by either model. The main point is that y and x are calibrated to approximate our computed $E°_{DFT}$ values to the Fds' experimental values. We will show below that this approach allows to predict redox potentials close to the experimental ones for the proximal FeS cluster in both the wt and C19G mutant of *E. coli* hydrogenase, for which the distance of ≈9 Å from bulk solvent resembles the above mentioned Fd R_p of 8.9 Å.

By applying Eq. S5 to $E°_{DFT}(-3/-2, -2/-1) = (-0.71, +0.09)$ and $E°_{Fd,exp}$ $(-3/-2, -2/-1) = (-0.41, +0.73)$, we obtain a set of two linear equations:

(1) $-0.41 = -0.71 + 7.72x + y$

(2) $+0.73 = +0.09 + 4.72x + y$

giving x = -0.113 and y = +1.175 eV. Interestingly, this value for x amounts to $\varepsilon_{av} = 78/(1-77\cdot x) \approx 8.0$, close to the value of 7.8 derived above solely from Perrin & Ichiye's parameters.[31] As explained above our value of y (+1.175 eV), which is larger than Perrin & Ichiye's computed Φ_p = 0.59 eV, results from a procedure that allows to correct for uncertainties in the DFT calculations.

For oxygen-sensitive hydrogenases, we expect that x = -0.113 and y +1.175 eV, as determined for Fds, will be appropriate to reach reasonable calculated values, given their similar $E°_{exp}$. In Eq. S5, x and y are anti-correlated: x < 0 because $\Delta E_{env}(w)$ is first computed for a water environment and then corrected by x to become ΔE_{env}(protein) with $4 < \varepsilon_{av} < 78$; y > 0 because the charge distribution around the anionic [4Fe-4S-4Sγ] cluster is predominantly positive. As x and y are of opposite sign, the estimation of $x\cdot\Delta E_{env}(w)+y$ in Eq. S5 (and therefore that of the computed vertical redox potentials) will be numerically robust. If we had used the estimated[27] value of $E°_{Fd,exp}$ (-2/-1) = +0.86 V (instead of 0.73 V) for our calibration, we would have obtained x = -0.157 (i.e. $\varepsilon_{av} \approx 6.0$) and y = +1.509 eV. In this case, the $[x\cdot\Delta E_{env}(w)+y]/F$ correction (Eq. S5) becomes 0.30 and 0.77 V for the (-3/-2) and (-2/-1) redox couples, respectively (instead of 0.30 and 0.64 V).

4) All the results compiled in **Tables S2** and **S3** suggested to us the use of the following strategy to *estimate* the redox potentials for *Ec*Hyd1:

i) compute the wt and C19G redox potentials for a dielectric continuum modelling water;

ii) correct the raw DFT *E*° values via Eq. S5 using (-3/-2) and (-2/-1) Fd experimental data. Below, we will apply this semi-empiric (se) correction to redox potentials computed for both wt and C19G models embedded in a water dielectric continuum and compare the relative redox potentials, in which we are interested, to focus on the direct effect of structural changes of the clusters. Using x = -0.113 and y = +1.175 and combining Eq. S1 with Eq. S2 we obtain:

$$E°_{DFT}(se) = \Delta E_B + \Delta E_{int} - T\Delta S + 0.887\Delta E_{env}(w) - 3.255 \qquad \text{(Eq. S6)}$$

(see the corresponding definitions in **ESI section 3**, with 1+x = 0.887 and $\Delta G_{SHE} + y = -3.255$)

5) The difference between (-3/-2) and (-2/-1) redox potentials computed for [4Fe-4S-4Sγ] models (see Table S2) is ~0.80 V (DFT, using ε_w =78) and ~1.20 V (experimental). Most of this difference is due to electronic *delocalization* within the mixed-valence pairs (see Mouesca *et al.* **1994**)[16]. As it turns out, at the DFT-XC VBP level, the stabilization energy within each delocalized ($Fe^{2.5+}$-$Fe^{2.5+}$) mixed-valence pair is ~0.5 eV for the current [4Fe-4S-4Sγ] models. This value is estimated to be half the bonding-antibonding energy difference of the delocalized electron within the mixed-valence pair. The -2 state exhibits two such ($Fe^{2.5+}$-$Fe^{2.5+}$) delocalized pairs whereas both the -1 and the -3 states have only one delocalized pair (associated with a ferric Fe^{3+}-Fe^{3+} or a ferrous Fe^{2+}-Fe^{2+} pair, respectively). As a consequence, the contribution of the electronic delocalization to the redox potentials' difference of the two (-3/-2) and (-2/-1) redox couples is ~1.0 V. As already discussed in Mouesca *et al.* **2013**,[32] even partial valence localization, i.e. breaking of the delocalization resonance within mixed-valence pairs, should significantly reduce this source of differential contribution to the redox potentials' difference in the case of proximal clusters from O_2-tolerant [NiFe]-hydrogenases. We will show below that this is indeed the case, due to their lack of symmetry.

4.2. Computed one-electron vertical redox potentials for the DFT geometry-optimized wt models.

We geometry-optimized in water (ε_w =78) the five wt models illustrated in **Scheme S2** for BS12 and BS13 states. An analysis of distances involving Fe ions (**Table S4**) shows that the experimental structures are reasonably well reproduced in the wt-pc_{red}-NH, wt-pc_{ox}-NH and wt-pc_{sox}-NFe models.

Table S4. Fe-Fe and Fe-ligand distances in crystal structures and geometry-optimized DFT models of the wt *Ec*Hyd1 proximal cluster.*

	Model	PC_{red}-X	pc_{red}-NH	PC_{ox}-X	pc_{ox}-NH	pc_{sox}-NH	PC_{sox}-X	pc_{ox}-NFe	pc_{sox}-NFe
atom	pair	(Å)	(Å)	(Å)	(Å)	(Å)	(Å)	(Å)	(Å)
Fe1	Fe2	2.6	2.7	2.6	2.7	2.6	2.6	2.5	2.6
Fe1	Fe3	3.6	3.4	3.6	3.5	**2.9**	3.6	3.6	3.7
Fe1	Fe4	2.8	2.7	2.7	2.6	2.6	3.1	2.9	2.7
Fe2	Fe3	2.8	2.7	2.7	2.7	2.6	2.7	2.7	2.7
Fe2	Fe4	2.8	2.6	3.0	2.6	2.6	3.9	**2.8**	3.5
Fe3	Fe4	4.0	**3.5**	4.2	**3.6**	**3.4**	5.3	**4.0**	**4.6**
Fe1	S1	2.3	2.2	2.3	2.2	2.2	2.3	2.2	2.3
	S2	2.3	2.3	2.3	2.3	2.2	2.3	2.3	2.3
	Cys17Sγ	2.3	2.3	2.3	2.2	2.2	2.3	2.3	2.2
	Cys19Sγ	2.3	2.3	2.3	2.3	2.3	2.4	2.3	2.3
Fe2	S1	2.3	2.3	2.3	2.3	2.2	2.3	2.2	2.3
	S2	2.3	2.2	2.3	2.2	2.2	2.3	2.2	2.3
	S3	2.3	2.3	2.2	2.3	2.2	2.2	2.3	2.2
	Cys115Sγ	2.3	2.3	2.3	2.3	2.2	2.3	2.3	2.3
Fe3	S2	2.3	2.3	2.3	2.3	2.2	2.3	2.2	2.2
	S3	2.3	2.2	2.3	2.2	2.2	2.3	2.3	2.2
	Cys120Sγ	2.4	2.3	2.3	2.3	2.2	2.3	2.3	2.3
	Cys149Sγ	2.3	2.3	2.3	2.3	2.2	2.3	2.3	2.3
Fe4	S1	2.3	2.3	2.3	2.3	2.2	2.5	2.2	2.2
	S3	2.4	2.3	2.8	2.3	2.2	4.0	**2.3**	4.0
	Cys19Sγ	2.4	2.3	2.2	2.3	2.3	2.3	2.3	2.3
	Cys20Sγ	2.3	2.3	2.3	2.3	2.2	2.3	2.2	2.3
	Cys20N	3.2	3.5	3.1	3.4	3.4	2.1	2.0	2.0

* distances deviating > 0.5 Å compared to the closest experimental structure are marked in bold.

The DFT models are further compared with the available crystal structures in **Fig. S5**. Because no atom was fixed in the geometry-optimizations, some large deviations are observed for atoms not

---

[32] JM Mouesca, JC Fontecilla-Camps & PA Amara, *Angew. Chem. Int. Ed Engl.* **2013**, *52*, 2002.

directly bound to the cluster, but the core regions, which are most important for the redox properties of the cluster, are quite similar.

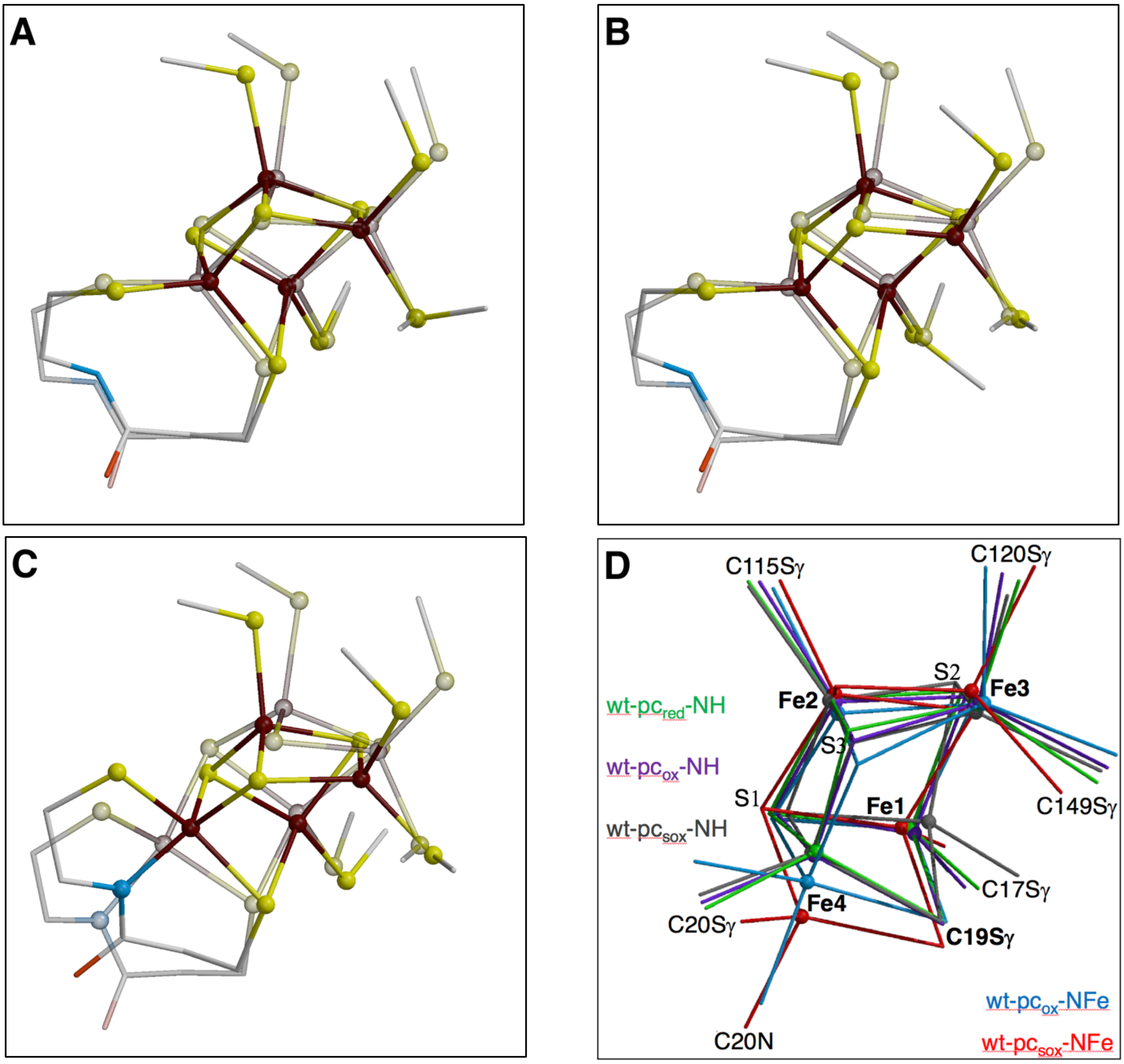

Figure S6. Structural comparison of geometry-optimized proximal cluster models for wt *Ec*Hyd1. (**A**) pc$_{red}$-NH and PC$_{red}$-X, (**B**) pc$_{ox}$-NH and PC$_{ox}$-X, (**C**) pc$_{sox}$-NFe and PC$_{sox}$-X, (**D**) superposition of the five DFT PC core models used for the redox potential calculations. The PC$_{red}$-X, PC$_{ox}$-X and PC$_{sox}$-X structures are shown in semi-transparent mode. Large shifts are observed for atoms outside the core, including not shown thiolate Cα atoms.

We used only the bonding energies of the lowest BS state for the *E*° calculation (see **Table S5**). Starting from the crystallographically determined wt-PC$_{red}$-X geometry we obtain the closely related **wt-pc$_{red}$-NH**. Upon oxidation, we obtain **wt-pc$_{ox}$-NH**, also close to its crystallographic wt-PC$_{ox}$-X counterpart. From here on, there are two possibilities: i) a second oxidation yields an unobserved wt-pc$_{sox}$-NH state that keeps its N-H bond, or ii) the amide N is deprotonated in the PC$_{ox}$ state, as an N-Fe bond is formed, yielding wt-pc$_{ox}$-NFe. Upon further oxidation, one finally obtains **wt-pc$_{sox}$-NFe**, with a distance between S$_{Cys19}$ and Fe3 of 4.34 Å for BS12 as compared to 4.54 Å in wt-PC$_{sox}$-X. In **Table S5**, we also show computed internal and entropic energy terms for the lowest BS state in each case. In the following discussion, we use the adjective "vertical" for one-electron redox potentials (see also **Scheme S2**).

Table S5. Bonding energies (E_B), internal energies (E_{int}), entropic terms (-TS at 298 K), solvation energies (E_{env}(w)) and resulting free energies (G, top = BS12, bottom = BS13) with calculated redox potentials ($E°_{DFT}$) for the best (**bold**) of BS12 or BS13 wt models before (at pH=0) and after correction (via Eq. S5). We also report relative G(se) values (using Eq. S7 without the $Q.\Phi_p'$ term) and d(S_{Cys19}-Fe3) distances (Fe3 designates the iron ion linked to Cys120 and Cys149).

wt models	Q	d(S_{C19}-Fe3) (Å)	E_B (eV)	E_{int} (eV)	-TS (eV)	E_{env}(w) (eV)	G (eV)	$E°_{DFT}$ (V)	G(se) (eV)	$E°_{DFT}$(se) (V)
wt-pc$_{red}$-NH	-3	3.59 (exp. 4.08)	-310.082	+12.18	-3.38	-13.75	-315.03		-313.48	
			-310.119	+12.10	-3.33	-14.05	**-315.40**	**-0.29**	**-313.81**	**+0.06**
wt-pc$_{ox}$-NH	-2	3.64 (exp. 4.25)	-313.300	+12.22	-3.39	-6.68	-311.15		-310.40	
			-313.426	+12.20	-3.30	-6.73	**-311.26**	**-0.07**	**-310.50**	**+0.62**
wt-pc$_{sox}$-NH	-1	3.36	-313.365	+12.33	-3.31	-2.42	-306.77		-306.50	
			-313.395	+12.31	-3.42	-2.39	**-306.90**		**-306.63**	
wt-pc$_{ox}$-NFe	-3	3.62	**-306.435**	+11.86	-3.42	-13.46	**-311.45**		**-309.93**	
			-306.317	+11.78	-3.18	-13.47	-311.19	**-0.12**	-309.66	**+0.27**
wt-pc$_{sox}$-NFe	-2	4.34 (exp. 4.54)	**-309.243**	+11.85	-3.28	-6.47	**-307.14**		**-306.41**	
			-309.240	+11.91	-3.35	-6.44	-307.12		-306.39	

It can be verified from the data in **Table S5** that:

i) The corrected (via Eq. S3) *vertical* redox potential for *protonated* wt-pc$_{red}$-NH/wt-pc$_{ox}$-NH is **+0.06 V** (using the lowest BS13 states), which is quite close to the experimental value of +0.03 V. The corrected *vertical* redox potential for *deprotonated* wt-pc$_{ox}$-NFe/wt-pc$_{sox}$-NFe is **+0.27 V** (using the lowest BS12 states) which is close to the experimental value of +0.23 V, although the latter value may also correspond to the *diagonal* wt-pc$_{ox}$-NH/wt-pc$_{sox}$-NFe couple (see point **ii** below). Our corrected data in **Table S5** might suggest that the second oxidation occurs *after* deprotonation of wt-PC$_{ox}$, because a second wt-PC$_{ox}$/wt-PC$_{sox}$ oxidation event -while keeping a *protonated* amide- would yield a much higher (corrected) potential of +0.62 V. Remark: had we used for both redox potentials the alternative BS states, we would have obtained -0.17 V (BS12) and +0.02 V (BS13), respectively. Although down-shifted compared to experiment, these latter values still correctly reproduce the experimental redox potential difference of 0.20 V.

ii) However, on the basis of DFT calculations alone, we cannot conclude that the wt-pc$_{ox}$-NFe state is a stable (potentially observable) intermediate. In fact, this intermediate would not exist if proton and electron transfer were coupled (CPET); in that case, the measured *E*° of 0.23V would correspond to the *diagonal* wt-pc$_{ox}$-NH/pc$_{sox}$-NFe redox couple (more on this in section 4.3).

iii) The difference between the two *uncorrected* redox potentials computed from the three *protonated* models is -0.07 – (-0.29) = 0.22 V, compared to 0.80 V in the case of symmetrical [4Fe-4S-4Sγ] clusters (**Table S3**). One sees here *the direct impact of partial valence localization in the asymmetrical proximal cluster*, which reduces by ~72 % the difference between the redox potential values relative to a symmetric cluster. This justifies in part the intuitive insight of Mouesca *et al.* **2013**,[30] although the mechanism proposed here puts forward an alternative route for the wt-PC$_{ox}$/wt-PC$_{sox}$ redox couple to further reduce the redox potential gap.

4.3. Deprotonation pathways for the DFT geometry-optimized wt models.

To compare two possible pathways, i.e., deprotonation of wt-PC$_{ox}$ followed by oxidation (coupled or not) *versus* oxidation followed by *horizontal* deprotonation (see **Scheme S2** and **Table S5**), we first thought of computing free energies for all the states. Using the same calibration for ΔE_{env} as in Eq. S6 (but neglecting the constant ΔG_{SHE} shift term that is needed only for *E*° *vertical* calculations) we would obtain for the cluster a relative free energy of:

$$G(se) = E_B + (1+x)E_{env} + E_{int} - TS + Q\cdot\Phi_p' \qquad \text{(Eq. S7)}$$

Notice that the new electrostatic term Φ_p' contains Φ_p (>0) which now contributes negatively to $\Delta G(se)$ when going from a protonated to a deprotonated proximal cluster as $Q \rightarrow Q-1$ (so $\Delta Q = -1$; the situation was the opposite upon oxidation with $Q \rightarrow Q+1$; cf. Eq. S5). After deprotonation there will be also a change in Φ_p (becoming Φ_p') if the accepting base lies within the protein. In addition, the oxidation of the [3Fe-4S] cluster is known to take place before PC superoxidation. Each of these two changes adds a positive charge to the protein environment. As a consequence, the Φ_p' term in Eq. S7 becomes an unknown electrostatic term. In the anaerobic redox titration performed by Roessler *et al.* (ref.2), we can only speculate about the identity of the base that is involved in the superoxidation process, but we know it is not a partially reduced oxygen species at the active site because the reaction was carried out anaerobically. *In vivo*, upon exposure of the enzyme to O_2, the final proton acceptor may be different, being possibly an active site bound O_2-derived intermediate. Because we do not know the identity and location of the base in the titration experiment, we are unable to calculate ΔG°'s for reactions that involve proton transfer.

Concerning the effective pKa of the C19 amide N atom near the proximal cluster, it is probably lower than its normally expected value of ≥ 17. For this pKa the corresponding $\Delta G°$ (= $0.059\Delta pK_a$) would be ≥ +0.31 eV (≥ 7.2 kcal.mol^{-1}). In the present case however, deprotonation of the amide in wt-pc$_{ox}$-NH is facilitated and may be concerted by the subsequent formation of the N-Fe bond, ultimately resulting in wt-pc$_{sox}$-NFe. Thus, breaking the N-H bond is compensated by making the N-Fe bond. This explains why in the protein the wt-pc$_{sox}$-NFe state is stable enough to prevent the amide N from breaking its bond with iron and recapturing a proton.

As explained at the end of Section 4.1, point 3, our calibration procedure for the computation of *vertical* redox potential values is numerically robust due to the compensatory effect of x and y, which have opposite signs.[33] However, without knowing the nature and position of the proton acceptor, we cannot quantitatively estimate *horizontal* ΔG° deprotonation values. Therefore, we will concentrate our efforts on the computation of *vertical* redox potential values and will not further pursue the characterization of the energetics of deprotonation.

Two main key factors determine two close oxidation potentials for oxygen-tolerant hydrogenases:

i) the asymmetrical geometry of their proximal cluster, regardless of its oxidation state, disrupts the electronic delocalization within the mixed-valence pairs, thereby reducing the gap between two successive redox potentials for *similar* cluster structures. For symmetrical clusters, this gap was 0.80 V (**Table S3**) to be compared to 0.22 V within the wt-pc-NH family in O_2 tolerant Hyd-1, before using the semi-empirical correction for the protein environment (**Table S5**).

ii) the cluster charges of wt-pc$_{red}$-NH and wt-pc$_{ox}$-NH are -3 and -2, respectively. Deprotonating wt-pc$_{ox}$-NH, which is energetically compensated by forming the N-Fe bond, may allow for the next redox couple wt-pc$_{ox}$-NFe/wt-pc$_{sox}$-NFe to function with the *same* set of cluster charges (-3/-2). The impact of the conservation of total cluster charges forces a question about the superoxidation mechanism proposed by I. Dance, which combines NH deprotonation with protonation of an inorganic PC sulfide.[34] Because this cluster opening oxidation reaction involves a (formal) intra-cluster proton transfer, this results in a -1 charge for the superoxidized state. From **Table S5**, we have for wt-pc$_{ox}$-NH (with charge of -2): $E_B + 0.89E_{env}(w) = -319.42$ eV. We constructed a geometry-optimized model of the superoxidized state proposed by I. Dance (which is structurally *significantly different* from our wt-pc$_{sox}$-NH) and computed for this species $E_B + 0.89E_{env}(w) = -314.38$ eV.[35] Excluding the small correction from E_{int} and $-TS$ terms, the difference gives an $E°_{DFT}$ of +1.78 V, a value much more positive than experimentally observed. This strongly suggests that intra cluster proton transfer is not a valid option in going from PC$_{ox}$ to PC$_{sox}$.

---

[33] With the alternative set of x=-0.157 and y=+1.509, one obtains for the last column of **Table S5** values of +0.07, +0.76 and +0.27 V, respectively

[34] I Dance, *Chem. Sci.* **2015**, *6*, 1433.

[35] $E_B = -312.53$ eV and $E_{env}(w) = -2.08$ eV for the BS12 state.

4.4. Computed redox potentials for the DFT geometry-optimized C19G models

For the C19G variant we obtained a somewhat different story. Using the same procedure as for the wt, the C19G variant models (**Scheme S3**) were first geometry-optimized in water (**Table S6, Fig. S7**), then in the gas phase to obtain bonding, solvation and internal energies, entropic terms and the resulting redox potentials for the lowest of BS12 and BS13 states (**Table S7**). We also explored the possibility of a further hyper-oxidation ("hox"), by adding "all ferric" (v-PC$_{\text{"hox"}}$) versions, including protonated–NH and deprotonated–NFe variants as illustrated in **Scheme S3**. Presumably because these have the same overall charge as the corresponding wt-PC$_{\text{sox}}$ states (see **Fig. 3** in main text), we observe that they could form stable, although unprecedented, cluster species. However, in the absence of experimental evidence for their existence, we will not further discuss these putative states.

v–pc$_{\text{"red"}}$-NH^{-4}
↓ ox (– e$^-$)
v–pc$_{\text{"ox"}}$-NH^{-3} -H$^+$ → **v–pc$_{\text{"ox"}}$-NFe^{-4}**
↓ ox (– e$^-$) ↓ ox (– e$^-$)
v–pc$_{\text{"sox"}}$-NH^{-2} -H$^+$ → **v–pc$_{\text{"sox"}}$-NFe^{-3}**
↓ ox (– e$^-$) ↓ ox (– e$^-$)
v–pc$_{\text{"hox"}}$-NH^{-1} -H$^+$ → **v–pc$_{\text{"hox"}}$-NFe^{-2}**

Scheme S3. Chemical relationships between geometry-optimized models of the *Ec*Hyd1 C19G variant. Compared to the wt (Scheme S2), charges of corresponding states are more negative by -1.

Table S6. Comparison of distances in the crystal structure and geometry-optimized DFT models of the C19G variant *Ec*Hyd1 proximal cluster.*

atom	Model pair	v-PC-X (Å)	v-pc$_{\text{"red"}}$-NH (Å)	v-pc$_{\text{"ox"}}$-NH (Å)	v-pc$_{\text{"ox"}}$-NFe (Å)	v-pc$_{\text{"sox"}}$-NH (Å)	v-pc$_{\text{"sox"}}$-NFe (Å)
Fe1	Fe2	2.5	2.7	2.6	2.7	2.6	2.7
Fe1	Fe3	3.4	3.5	3.4	3.8	3.3	3.8
Fe1	Fe4	2.7	2.6	2.6	2.7	2.6	2.7
Fe2	Fe3	2.8	2.7	2.7	2.7	2.7	2.7
Fe2	Fe4	2.8	2.6	2.7	**3.6**	2.7	**3.8**
Fe3	Fe4	3.8	**3.3**	3.6	**4.9**	3.6	**5.0**
Fe1	S1	2.3	2.2	2.3	2.3	2.3	2.3
	S2	2.2	2.4	2.3	2.3	2.3	2.3
	S4	2.2	2.2	2.2	2.2	2.2	2.2
	Cys17Sγ	2.3	2.3	2.3	2.3	2.2	2.3
Fe2	S1	2.3	2.3	2.3	2.3	2.2	2.3
	S2	2.2	2.2	2.3	2.3	2.3	2.3
	S3	2.3	2.3	2.2	2.2	2.2	2.2
	Cys115Sγ	2.2	2.3	2.3	2.3	2.2	2.3
Fe3	S2	2.3	2.3	2.2	2.2	2.2	2.2
	S3	2.3	2.2	2.3	2.2	2.3	2.2
	Cys120Sγ	2.4	2.3	2.3	2.3	2.3	2.3
	Cys149Sγ	2.2	2.3	2.3	2.3	2.3	2.3
Fe4	S1	2.3	2.3	2.2	2.2	2.2	2.2
	S3	2.4	2.3	2.3	**4.1**	2.3	**4.5**
	S4	2.2	2.2	2.2	2.2	2.2	2.2
	Cys20Sγ	2.3	2.3	2.3	2.3	2.3	2.3
	Cys20N	3.5	**4.0**	**4.0**	**2.1**	3.9	**2.0**

* distances deviating > 0.5 Å compared to the v-PC-X structure are marked in bold.

Like for the wt, we compared the distances involving Fe ions for the crystal structure and the geometry-optimized models (**Table S6**), showing that the novel [4Fe-4S-5Sγ] cluster is best reproduced in the v-pc$_{\text{"ox"}}$-NH and v-pc$_{\text{"sox"}}$-NH models. This is further confirmed in the structural superpositions shown in **Fig. S7**. The DFT models with an N-Fe bond, v–pc$_{\text{"ox"}}$-NFe and v–pc$_{\text{"sox"}}$-NFe, resemble wt-pc$_{\text{sox}}$-NFe (see also **Table S5** and **Fig. S6d**).

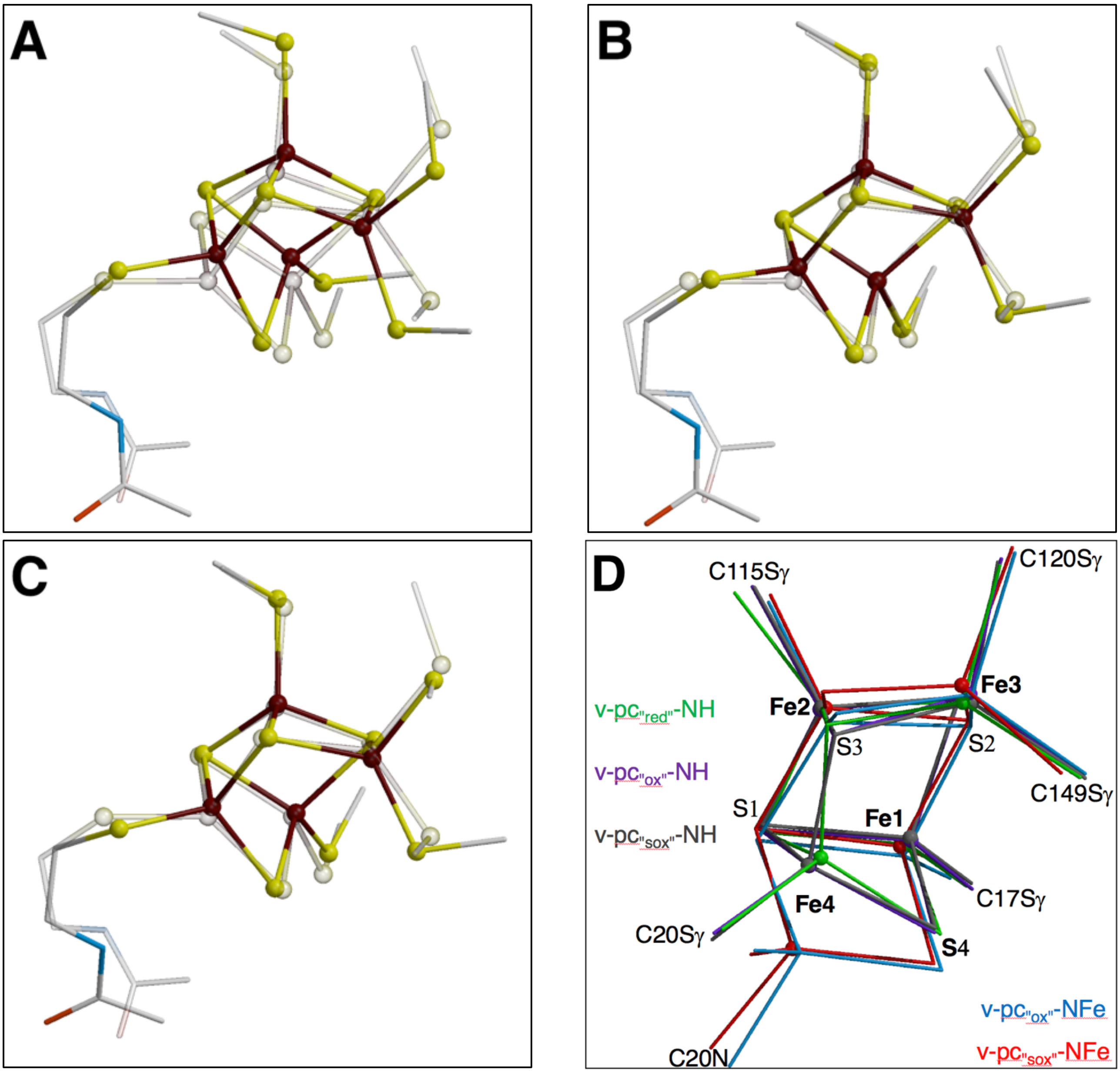

Figure S7. Comparison of geometry-optimized proximal cluster models for the *Ec*Hyd1 C19G variant with the crystal structure. (**A**) v-pc$_{\text{"red"}}$-NH, (**B**) v-pc$_{\text{"ox"}}$-NH, (**C**) v-pc$_{\text{"sox"}}$-NH. (**D**) superposition of the five DFT PC core models used for the redox potential calculations. The crystal structure of the variant is shown in semi-transparent mode, colors are as in **Fig. S6**. In order to simplify the figure thiolate Cα atoms displaying large shifts are not shown.

The results of the redox potential calculations are compiled in **Table S7**, which shows that:

i) Compared to the DFT-computed redox potentials for wt, only one potential is predicted to be reachable under physiological conditions, i.e. that of the redox couple of the protonated models v-pc$_{\text{"ox"}}$-NH and v-pc$_{\text{"sox"}}$-NH with a corrected (*vertical*) value = **+0.23** V. This value is in good agreement with the experimental one of 0.240±0.015 V (see **Section S1**). The v-pc$_{\text{"red"}}$-NH/v-pc$_{\text{"ox"}}$-NH redox couple (corrected) value of -0.62 V is quite negative, which probably explains why the v-PC$_{red}$ state is not observed experimentally and the C19G variant is not O_2-tolerant.

ii) After deprotonation of the amide, the calculated v-pc$_{\text{"ox"}}$-NFe/v-pc$_{\text{"sox"}}$-NFe (*vertical)* redox couple corrected *E*° value is negative: -0.38 V, compared to +0.27 V for the corresponding wt states. This different result is due to the more negative cluster charges involved (-4/-3 in the variant, -3/-2 in wt).

As for wt-pc states - and in the absence of crystallographic evidence for the formation of an N-Fe bond in the C19G variant - we will not pursue the energetics of deprotonation of the amide N at the present stage of our investigation.

Table S7. Bonding energies (E_B; top = BS12, bottom = BS13), internal energies (E_{int}), entropic terms (-TS at 298 K), solvation energies (E_{env}(w) and the resulting free energies (G, top = BS12, bottom = BS13) and calculated redox potentials ($E°_{DFT}$) for the best (**bold**) of BS12 or BS13 wt models before (at pH=0) and after correction (via Eq. S3). We also report d(S4-Fe3) distances where Fe3 is the iron ion linked to both Cys120 and Cys149 and S4 is the inorganic sulfur anion replacing the thiolate sulfur of Cys19 (see **Fig. 1B** in main text).

mutant models	**Q**	**d(S4-Fe3) (Å)**	**E_B (eV)**	**E_{int} (eV)**	**-TS (eV)**	**E_{env}(w) (eV)**	**G (eV)**	**$E°_{DFT}$ (V)**	**G(se) (eV)**	**$E°_{DFT}$(se) (V)**
v-pc$_{\text{"red"}}$-NH	-4	3.69	-292.488 **-292.555**	+11.39	-3.06	-23.64 -23.74	**-307.97**	-0.65	**-305.29**	**-0.62**
v-pc$_{\text{"ox"}}$-NH	-3	3.80 (exp. 4.00)	**-298.768** -298.758	+11.58	-3.27	-13.75 -13.73	**-304.21**	-0.12	**-302.66**	**+0.23**
v-pc$_{\text{"sox"}}$-NH	-2	3.60	**-301.777** -301.629	+11.71	-3.40	-6.43 -6.58	**-299.90**		**-299.17**	
v-pc$_{\text{"ox"}}$-NFe	-4	4.54	**-288.884** -288.698	+11.10	-3.06	-23.22 -22.14	**-304.06**	-0.41	**-301.44**	**-0.38**
v-pc$_{\text{"sox"}}$-NFe	-3	4.61	**-294.790** -294.465	+11.27	-3.26	-13.29 -13.05	**-300.07**		**-298.57**	

To summarize this comparison of the redox potentials of wt and C19G-Hyd-1 we conclude that:

i) for wt, PC$_{red}$-**NH**/PC$_{ox}$-**NH** and PC$_{ox}$-**NFe**/PC$_{sox}$-**NFe** redox potentials are comparable because they involve the same set of cluster charges (-3/-2) and deprotonation of the amide is energetically compensated by the probably concerted formation of the N-Fe bond. Moreover, the two computed values (+0.06 and 0.27 V) match the experimental ones (+0.03 and 0.23 V), showing the same difference of 0.2 V. However, we do not exclude that the experimentally obtained superoxidation potential corresponds to the PC$_{ox}$-**NH/**PC$_{sox}$-**NFe** pair involving proton-coupled electron transfer (PCET), with a contribution for the proton transfer process that we cannot calculate because of the unknown identity of the proton acceptor in the anaerobic EPR experiment (Fig. S1).

ii) for the C19G variant, both v-pc$_{\text{"red"}}$-**NH**/v-pc$_{\text{"ox"}}$-**NH** and v-pc$_{\text{"ox"}}$-**NFe**/v-pc$_{\text{"sox"}}$-**NFe** computed redox potentials are relatively close but negative: -0.62 and -0.38 V, respectively, with a difference of 0.24 V, because they involve the same set of -4/-3 cluster charges. The closest redox potential value to the experimentally observed one (+0.24V) is obtained for the v-pc$_{\text{"ox"}}$-**NH**/v-pc$_{\text{"sox"}}$-**NH** couple (+0.23V).